Supporting Information:

Chemical Trends in the Lattice Thermal Conductivity of Li(Ni, Mn, Co)O$_2$ (NMC) Battery Cathodes

Hui Yang,[†,#] Christopher N. Savory,[‡,#] Benjamin J. Morgan,[¶,#] David O. Scanlon,[‡,§,#] Jonathan M. Skelton,[∗,‖] and Aron Walsh[∗,†,⊥,#]

†Department of Materials, Imperial College London, Exhibition Road, London SW7 2AZ, UK

‡University College London, Department of Chemistry and Thomas Young Centre, 20 Gordon Street, London WC1H 0AJ, UK

¶Department of Chemistry, University of Bath, Claverton Down, Bath BA2 7AY, UK

§Diamond Light Source Ltd., Diamond House, Harwell Science and Innovation Campus, Didcot, Oxfordshire OX11 0DE, UK

‖Department of Chemistry, University of Manchester, Oxford Road, Manchester M13 9PL, UK

⊥Department of Materials Science and Engineering, Yonsei University, Seoul 03722, Korea

#The Faraday Institution, Quad One, Harwell Science and Innovation Campus, Didcot, UK

E-mail: jonathan.skelton@manchester.ac.uk; a.walsh@imperial.ac.uk

Mesh convergence tests

To identify appropriate lifetime-sampling meshes for calculating the thermal conductivity, explicit convergence tests were performed for each of the three compounds where the sampling mesh was systematically increased until convergence of the room-temperature averaged lattice thermal conductivity $\kappa_{\text{ave}} = \frac{1}{3}(\kappa_{xx} + \kappa_{yy} + \kappa_{zz})$ was obtained. For $LiCoO_2$ and $LiNiO_2$ the three reciprocal lattice vectors b are similar/identical in length and therefore isotropic meshes with $nb_1 = nb_2 = nb_3$ were used, whereas for $LiMnO_2$ $|b_1| \approx 2|b_2| \approx 4|b_3|$ and sampling meshes for which $nb_1 = 2nb_2 = 4nb_3$ were tested.

The convergence tests for $LiCoO_2$, $LiNiO_2$ and $LiMnO_2$ are presented in Figures S1 - S4 and Tables S1 - S4. Based on this data, we selected $15 \times 15 \times 15$ meshes for $LiCoO_2$ and $LiNiO_2$ and a $16 \times 8 \times 4$ mesh for $LiMnO_2$ - these produce values of the 300 K κ_{ave} within 2.5 % of the largest meshes tested while substantially reducing the time needed to perform the post processing, which is important given that a large number of additional post-processing runs are required to study the ternary NMC system.

Note that two sets of calculations were performed for $LiNiO_2$ with displacement step sizes of 3×10^{-2} Å and 2×10^{-2} Å, and convergence tests were carried out on both.
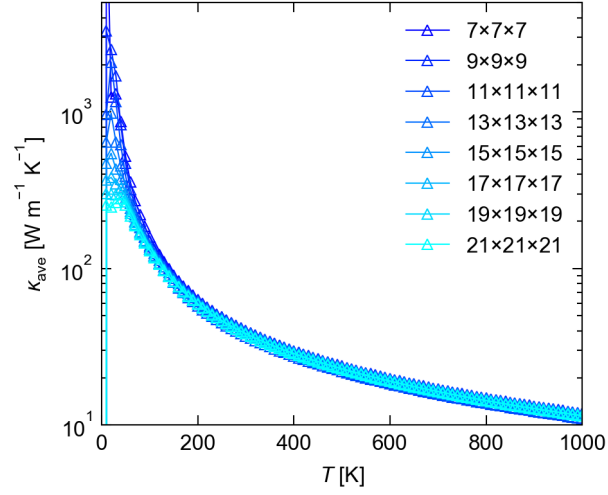
Figure S1: Convergence of the averaged lattice thermal conductivity $\kappa_{\mathrm{ave}} = \frac{1}{3}(\kappa_{xx} + \kappa_{yy} + \kappa_{zz})$ of $LiCoO_2$ with respect to the Brillouin zone sampling mesh.
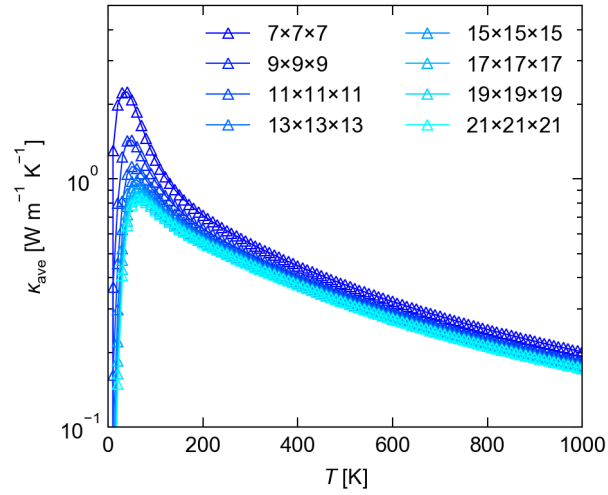

Figure S2: Convergence of the averaged lattice thermal conductivity $\kappa_{\mathrm{ave}} = \frac{1}{3}(\kappa_{xx} + \kappa_{yy} + \kappa_{zz})$ of $LiNiO_2$ (3×10^{-2} Å displacement step) with respect to the Brillouin zone sampling mesh.
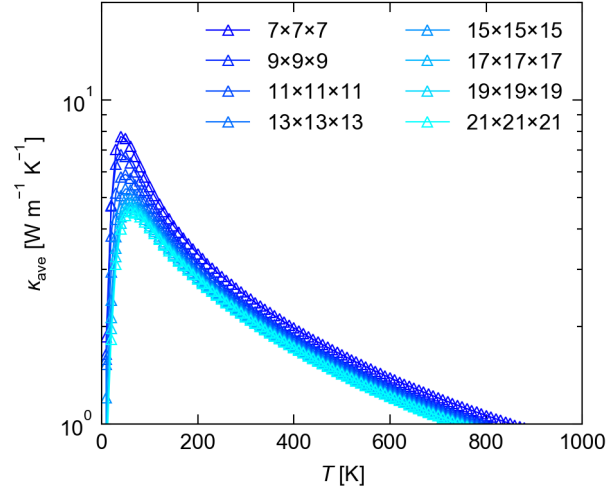
Figure S3: Convergence of the averaged lattice thermal conductivity $\kappa_{\mathrm{ave}} = \frac{1}{3}(\kappa_{xx}+\kappa_{yy}+\kappa_{zz})$ of LiNiO$_2$ (2×10^{-2} Å displacement step) with respect to the Brillouin zone sampling mesh.
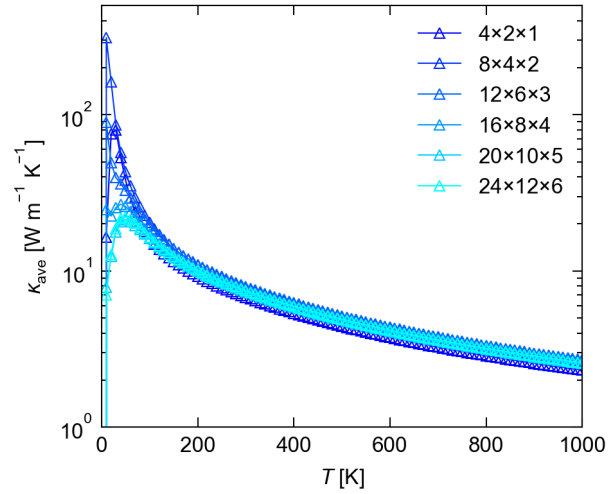

Figure S4: Convergence of the averaged lattice thermal conductivity $\kappa_{\mathrm{ave}} = \frac{1}{3}(\kappa_{xx}+\kappa_{yy}+\kappa_{zz})$ of LiMnO$_2$ with respect to the Brillouin zone sampling mesh.

Table S1: 300 K lattice thermal conductivity of LiCoO$_2$ obtained with each of the Brillouin zone sampling meshes shown in Figure S1. For each sampling mesh, the number of irreducible grid points (GPs) on the mesh is shown together with the κ_{xx}, κ_{yy} and κ_{zz} components of lattice thermal conductivity and the average κ_{ave}. The mesh selected for production calculations is marked with an asterisk (*). κ are given in W m^{-1} K^{-1}.

Mesh	# GPs	$\kappa_{xx} = \kappa_{yy}$	κ_{zz}	κ_{ave}	$\delta\kappa_{\text{ave}}$ [%]
$7 \times 7 \times 7$	44	53.74	12.37	39.95	4.39
$9 \times 9 \times 9$	85	55.24	10.03	40.17	4.97
$11 \times 11 \times 11$	146	50.76	9.68	37.06	-3.15
$13 \times 13 \times 13$	231	54.68	9.35	39.57	3.41
$15 \times 15 \times 15$ [*]	344	52.92	8.77	38.20	-0.18
$17 \times 17 \times 17$	489	53.73	8.54	38.67	1.04
$19 \times 19 \times 19$	670	53.60	8.39	38.53	0.69
$21 \times 21 \times 21$	891	53.32	8.16	38.27	0.00

Table S2: 300 K lattice thermal conductivity of LiNiO$_2$ (3×10^{-2} Å displacement step) obtained with each of the Brillouin zone sampling meshes shown in Figure S2. For each sampling mesh, the number of irreducible grid points (GPs) on the mesh is shown together with the κ_{xx}, κ_{yy} and κ_{zz} components of lattice thermal conductivity and the average κ_{ave}. The mesh selected for production calculations is marked with an asterisk (*). κ are given in W m^{-1} K^{-1}.

Mesh	# GPs	κ_{xx}	κ_{yy}	κ_{zz}	κ_{ave}	$\delta\kappa_{\text{ave}}$ [%]
$7 \times 7 \times 7$	172	0.429	0.745	0.475	0.550	22.07
$9 \times 9 \times 9$	365	0.343	0.719	0.423	0.495	9.95
$11 \times 11 \times 11$	666	0.330	0.692	0.412	0.478	6.13
$13 \times 13 \times 13$	1,099	0.317	0.679	0.401	0.466	3.37
$15 \times 15 \times 15$ [*]	1,688	0.308	0.671	0.394	0.458	1.60
$17 \times 17 \times 17$	2,457	0.306	0.668	0.393	0.456	1.18
$19 \times 19 \times 19$	3,430	0.303	0.660	0.390	0.451	0.10
$21 \times 21 \times 21$	4,631	0.301	0.662	0.388	0.450	0.00

Table S3: 300 K lattice thermal conductivity of $LiNiO_2$ (2×10^{-2} Å displacement step) obtained with each of the Brillouin zone sampling meshes shown in Figure S3. For each sampling mesh, the number of irreducible grid points (GPs) on the mesh is shown together with the κ_{xx}, κ_{yy} and κ_{zz} components of lattice thermal conductivity and the average κ_{ave}. The mesh selected for production calculations is marked with an asterisk (*). κ are given in $\mathrm{W\,m^{-1}\,K^{-1}}$.

Mesh	# GPs	κ_{xx}	κ_{yy}	κ_{zz}	κ_{ave}	$\delta\kappa_{\mathrm{ave}}$ [%]
$7 \times 7 \times 7$	172	1.708	3.558	2.217	2.494	16.24
$9 \times 9 \times 9$	365	1.546	3.384	2.076	2.335	8.85
$11 \times 11 \times 11$	666	1.500	3.312	2.026	2.279	6.23
$13 \times 13 \times 13$	1,099	1.461	3.220	1.997	2.226	3.75
$15 \times 15 \times 15$ [*]	1,688	1.430	3.183	1.958	2.190	2.07
$17 \times 17 \times 17$	2,457	1.414	3.158	1.944	2.172	1.23
$19 \times 19 \times 19$	3,430	1.401	3.135	1.930	2.155	0.45
$21 \times 21 \times 21$	4,631	1.390	3.129	1.918	2.146	0.00

Table S4: 300 K lattice thermal conductivity of $LiMnO_2$ obtained with each of the Brillouin zone sampling meshes shown in Figure S4. For each sampling mesh, the number of irreducible grid points (GPs) on the mesh is shown together with the κ_{xx}, κ_{yy} and κ_{zz} components of lattice thermal conductivity and the average κ_{ave}. The mesh selected for production calculations is marked with an asterisk (*). κ are given in $\mathrm{W\,m^{-1}\,K^{-1}}$.

Mesh	# GPs	κ_{xx}	κ_{yy}	κ_{zz}	κ_{ave}	$\delta\kappa_{\mathrm{ave}}$ [%]
$4 \times 2 \times 1$	6	11.64	5.59	3.11	6.78	-9.65
$8 \times 4 \times 2$	36	14.44	5.12	3.82	7.79	3.77
$12 \times 6 \times 3$	110	15.45	4.81	3.63	7.96	6.09
$16 \times 8 \times 4$ [*]	260	14.36	4.65	3.48	7.50	-0.09
$20 \times 10 \times 5$	502	14.39	4.45	3.30	7.38	-1.68
$24 \times 12 \times 6$	868	14.68	4.49	3.35	7.51	0.00

Force-constant symmetrisation

In these calculations, we found that the calculated 2nd- and 3rd-order interatomic force constants (IFCs) exhibited a significant amount of drift (Table S6). A basic assessment of the quantitative impact of the drift can be made by comparing thermal-conductivity curves obtained with and without symmetrising the force constants (Table S6, Figures S5 - S8).

For $LiCoO_2$ and $LiMnO_2$, symmetrisation increases the averaged 300 K thermal conductivity by 25% and 20 % respectively. On the other hand, the third-order IFCs calculated for $LiNiO_2$ using the same 3×10^{-2} Å displacement step size have a much larger drift, and symmetrisation increases the predicted 300 K κ by more than an order of magnitude. Reducing the step size to 2×10^{-2} Å reduces the drift and increases the unsymmetrised κ by a factor of four, although the drift remains an order of magnitude higher than in the $LiCoO_2$ and $LiMnO_2$ calculations. The symmetrised results of 6.16 and 5.78 $W\,m^{-1}\,K^{-1}$ obtained from the two sets of calculations on $LiNiO_2$ are similar, however, providing some confidence that the symmetrised results can be used for a semi-quantitative comparison of the three systems.

As noted in the text, we therefore opted to use the $LiNiO_2$ calculations performed with the smaller 2×10^{-2} Å step size in our analysis.

Table S5: Maximum drift in the calculated 2nd-order force constants of $LiCoO_2$, $LiNiO_2$ and $LiMnO_2$ reported by Phonopy and the 2nd- and 3rd-order force constants (FC2/FC3) reported by Phono3py, together with the averaged 300 K lattice thermal conductivity κ_{ave} obtained with and without force-constant symmetrisation. The κ_{ave} were computed using the sampling meshes identified in the previous section. Two sets of values are given for $LiNiO_2$ for Phono3py calculations performed with finite-displacement step sizes of 3×10^{-2} and 2×10^{-2} Å. κ_{ave} are given in in $W\,m^{-1}\,K^{-1}$.

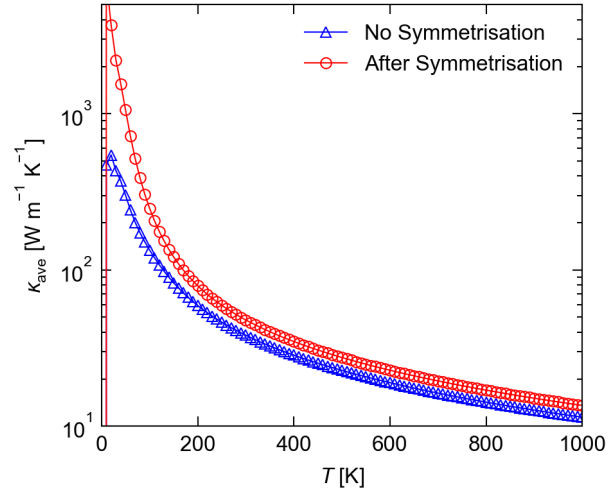| | | Max. Drift | | κ_{ave} | |
System	Phonopy	Phono3py (FC2)	Phono3py (FC3)	Unsymmetrised	Symmetrised
$LiCoO_2$	1.09×10^{-1}	5.09×10^{-2}	-3.10	38.20	47.83
$LiNiO_2$	3.58×10^{-1}	1.26×10^{-1}	-65.0	0.458	5.78
		3.66×10^{-1}	24.6	2.19	6.16
$LiMnO_2$	-3.18×10^{-1}	1.78×10^{-1}	-2.49	7.50	8.99

Figure S5: Averaged lattice thermal conductivity of $LiCoO_2$ as a function of temperature calculated without (blue triangles) and with force constant symmetrisation (red circles) using the sampling mesh selected in the previous section.
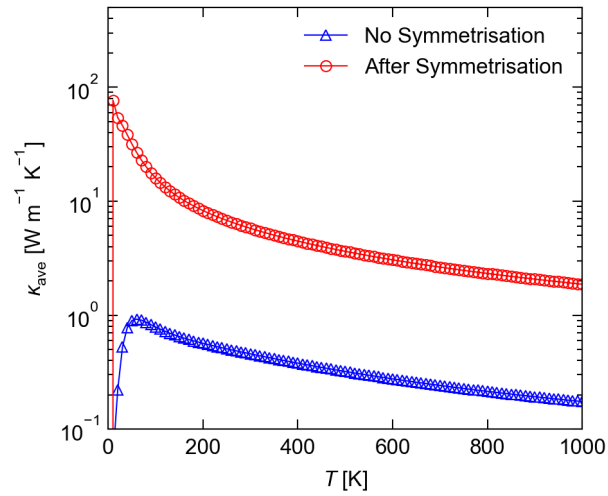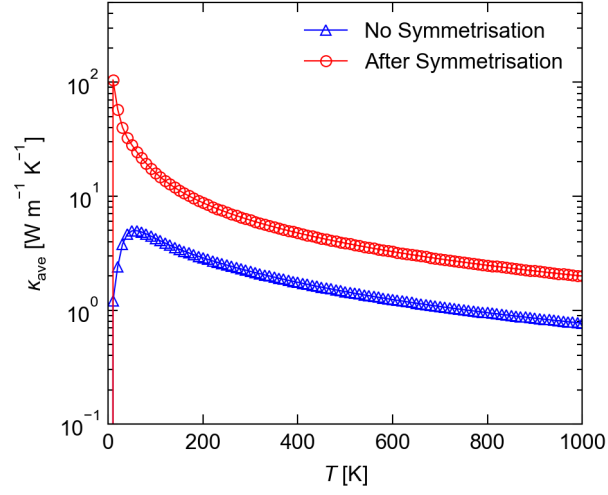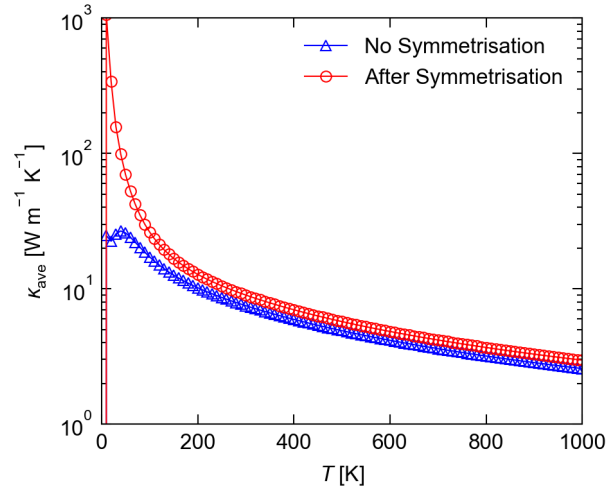

Figure S6: Averaged lattice thermal conductivity of $LiNiO_2$ (3×10^{-2} Å displacement step) as a function of temperature calculated without (blue triangles) and with force constant symmetrisation (red circles) using the sampling mesh selected in the previous section.

Figure S7: Averaged lattice thermal conductivity of $LiNiO_2$ (2×10^{-2} Å displacement step) as a function of temperature calculated without (blue triangles) and with force constant symmetrisation (red circles) using the sampling mesh selected in the previous section.

Figure S8: Averaged lattice thermal conductivity of $LiMnO_2$ as a function of temperature calculated without (blue triangles) and with force constant symmetrisation (red circles) using the sampling mesh selected in the previous section.

Force-constant range convergence tests

The 3rd-order interatomic force constants (IFCs) $\Phi_{\alpha\beta\gamma}$ are defined as:

$$\Phi_{\alpha\beta\gamma}(jl, j'l', j''l'') = \frac{\partial^3 E}{\partial r_\alpha(jl)\partial r_\beta(j'l')\partial r_\gamma(j''l'')} = -\frac{\partial^2 F_\alpha(jl)}{\partial r_\beta(j'l')\partial r_\gamma(j''l'')} \tag{1}$$

where α, β and γ label the Cartesian directions and the indices j and l label atoms and unit cells, respectively.

The IFCs are computed using finite differences by performing pairwise displacements of atoms $j'l'$ and $j''l''$ and computing the resulting force on atom jl. The number of displacements needed to evaluate the full set of IFCs scales with the size of the supercell and can quickly become unmanageable for large cells. For $LiCoO_2$ and $LiNiO_2$, computing the full set of IFCs in a $2 \times 2 \times 2$ supercell expansion requires 452 and 2,316 displacements, respectively, while computing the IFCs for LiMnO2 using a $3 \times 1 \times 1$ supercell requires 6,936 displacements. If the supercells for $LiCoO_2$ and $LiNiO_2$ are increased to $3 \times 3 \times 3$ expansions, the number of required displacements is increased to 1,444 and 7,788 respectively. Similarly, using $4 \times 1 \times 1$, $3 \times 2 \times 1$ or $4 \times 2 \times 1$ supercells for $LiMnO_2$ requires 9,240, 13,848 and 18,456 displacements, respectively. We note that the cost of computing the forces in larger supercells also scales with the size, and that this scaling is significantly higher for non-local hybrid functionals such as HSE 06, as used in this work, than for (semi-)local DFT functionals based on the LDA and GGA forms.

It is generally the case that the range of the 3rd-order interaction in real space is smaller than the 2nd-order interaction. A technique employed in many studies is therefore to impose a cutoff range beyond which the $\Phi_{\alpha\beta\gamma}$ are assumed to be zero. The cutoff may be defined in terms of a distance between the reference and displaced atoms, or, more commonly, in terms of a number of nearest neighbours.

To check convergence with respect to range, we performed a series of calculations in which the thermal conductivity was calculated with a range cutoff of $r_{\text{cut}} = 2$-5 Å imposed

on the 3rd-order IFCs. r_{cut} is defined here such that if the distance between any pair of atoms in the triplet jl, $j'l'$ and $j''l''$ is larger than r_{cut} the corresponding $\Phi_{\alpha\beta\gamma}$ is set to zero (c.f. Equation (1)). Tests on $LiCoO_2$, $LiNiO_2$ (2×10^{-2} Å displacement step) and $LiMnO_2$ are shown in Figs. S9, S10 and S11 respectively.

For $LiCoO_2$ and $LiMnO_2$, we find that the averaged thermal conductivity κ_{ave} converges rapidly as a function of distance, such that a cutoff of $r_{\mathrm{cut}} = 2.5$ Å, which includes the first six nearest neighbours of all the atoms, yields 300 K values within 10-15 % of those obtained using the full set of IFCs defined in the chosen supercell expansions. On the other hand, for $LiNiO_2$ the convergence appears to be slower, and even with $r_{\mathrm{cut}} = 3.5$ Å, which includes 12-16 nearest neighbours, the calculated κ_{ave} is still in error by > 30 % compared to the reference value obtained with no cutoff.

Interestingly, we also find that the convergence with respect to the interaction range appears to be faster when force-constant symmetrisation is applied to improve the numerical accuracy of the derivatives in Equation (1). This is likely to be an artefact of numerical noise - i.e. using a larger cutoff distance and including more IFCs reduces the "average" level of noise - but again underscores the potential impact of drift if not carefully checked, as seen in the previous section.

Overall, however, these tests suggest that our chosen supercell sizes all include 3rd-order IFCs to a sufficient range to converge the calculated thermal conductivity, and are therefore a good balance between accuracy and computational cost.
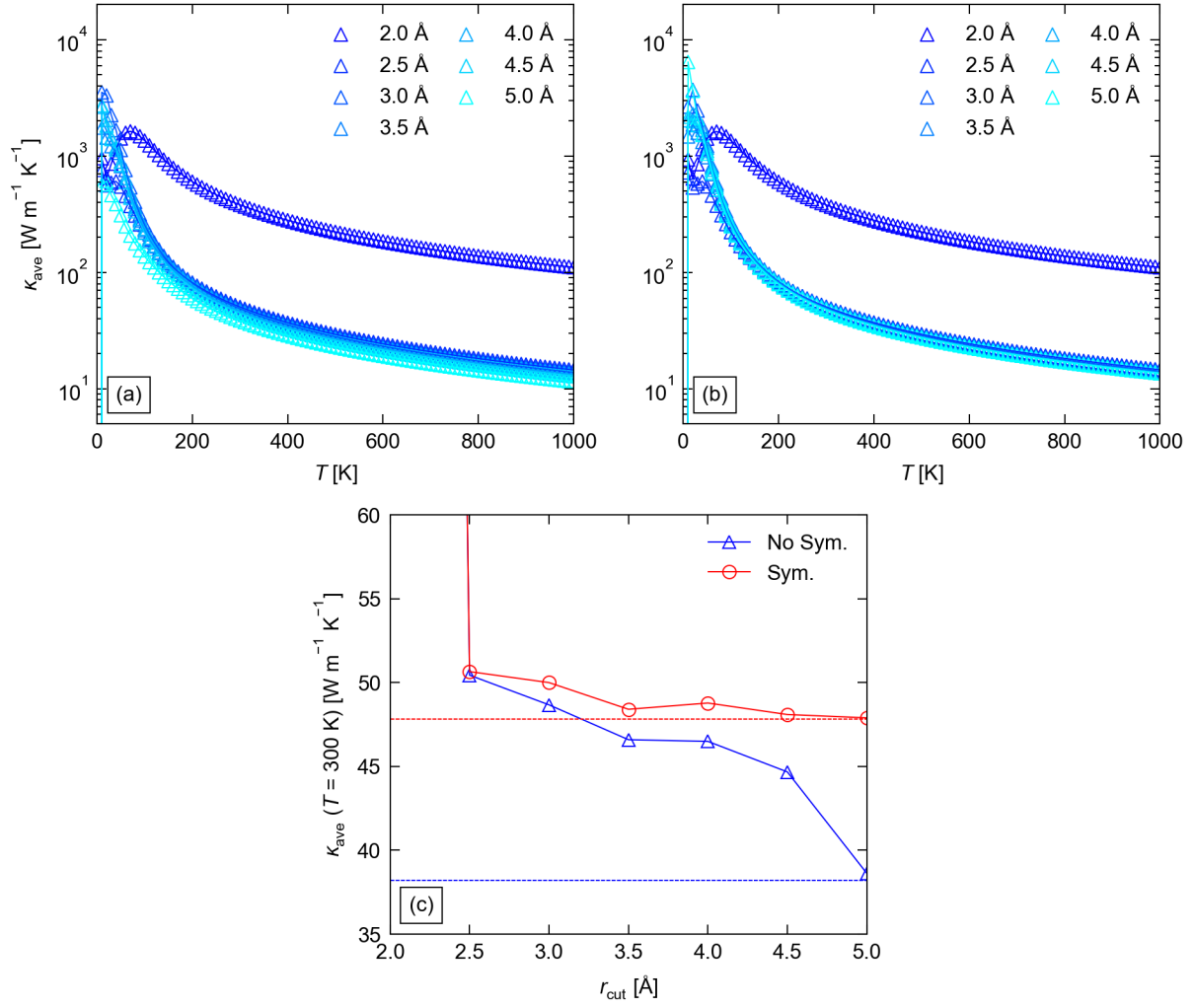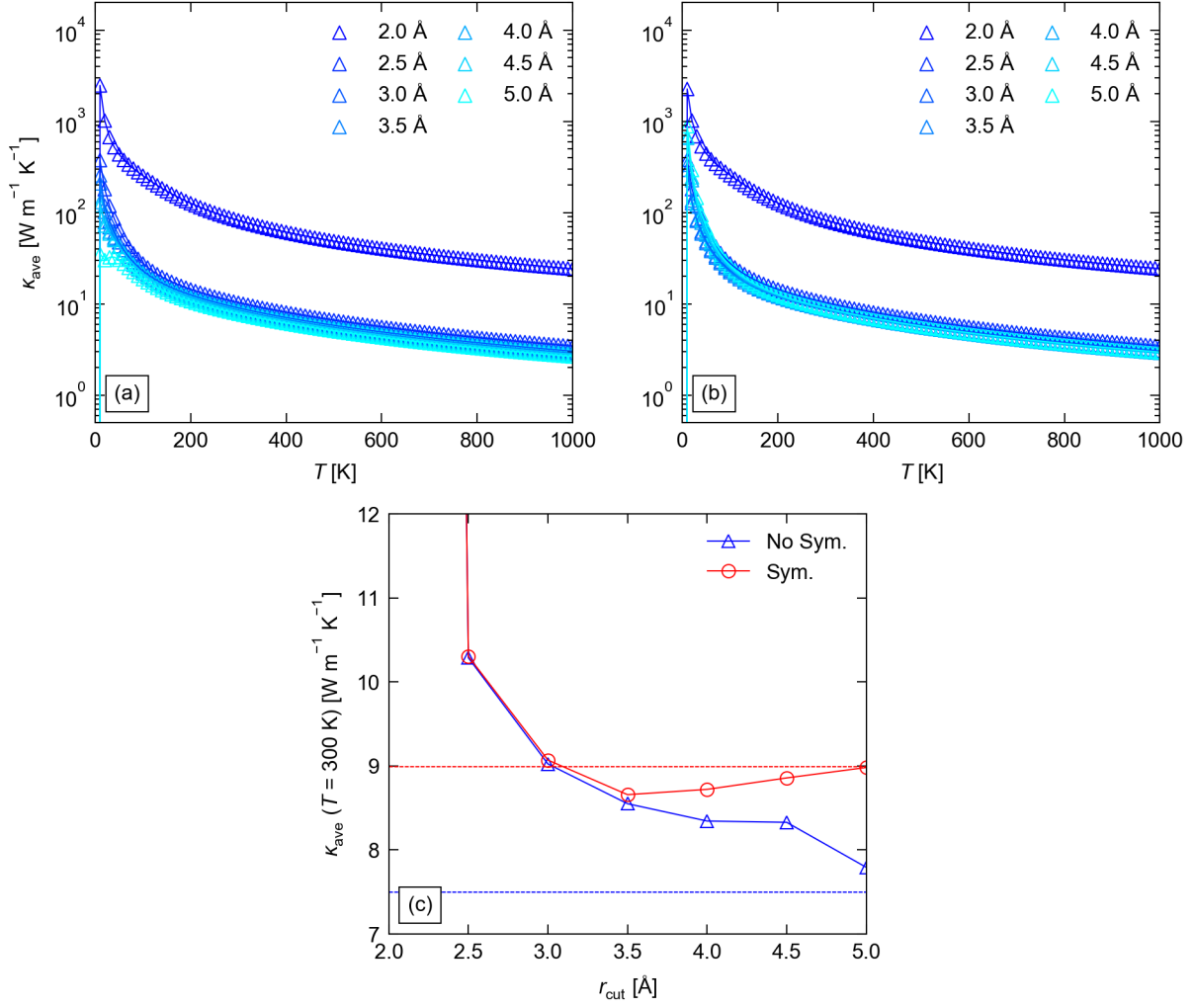
Figure S9: Convergence of the averaged lattice thermal conductivity of $LiCoO_2$ as a function of the 3rd-order interaction cutoff r_{cut}. (a)/(b) κ_{ave} as a function of temperature computed with r_{cut} = 2-5 Å without (a) and with (b) symmetrisation applied to the IFCs to reduce numerical noise. (c) 300 K κ_{ave} as a function of r_{cut} computed with and without force-constant symmetrisation. The dashed lines show the reference values obtained using the full set of 3rd-order IFCs defined in our chosen supercells.
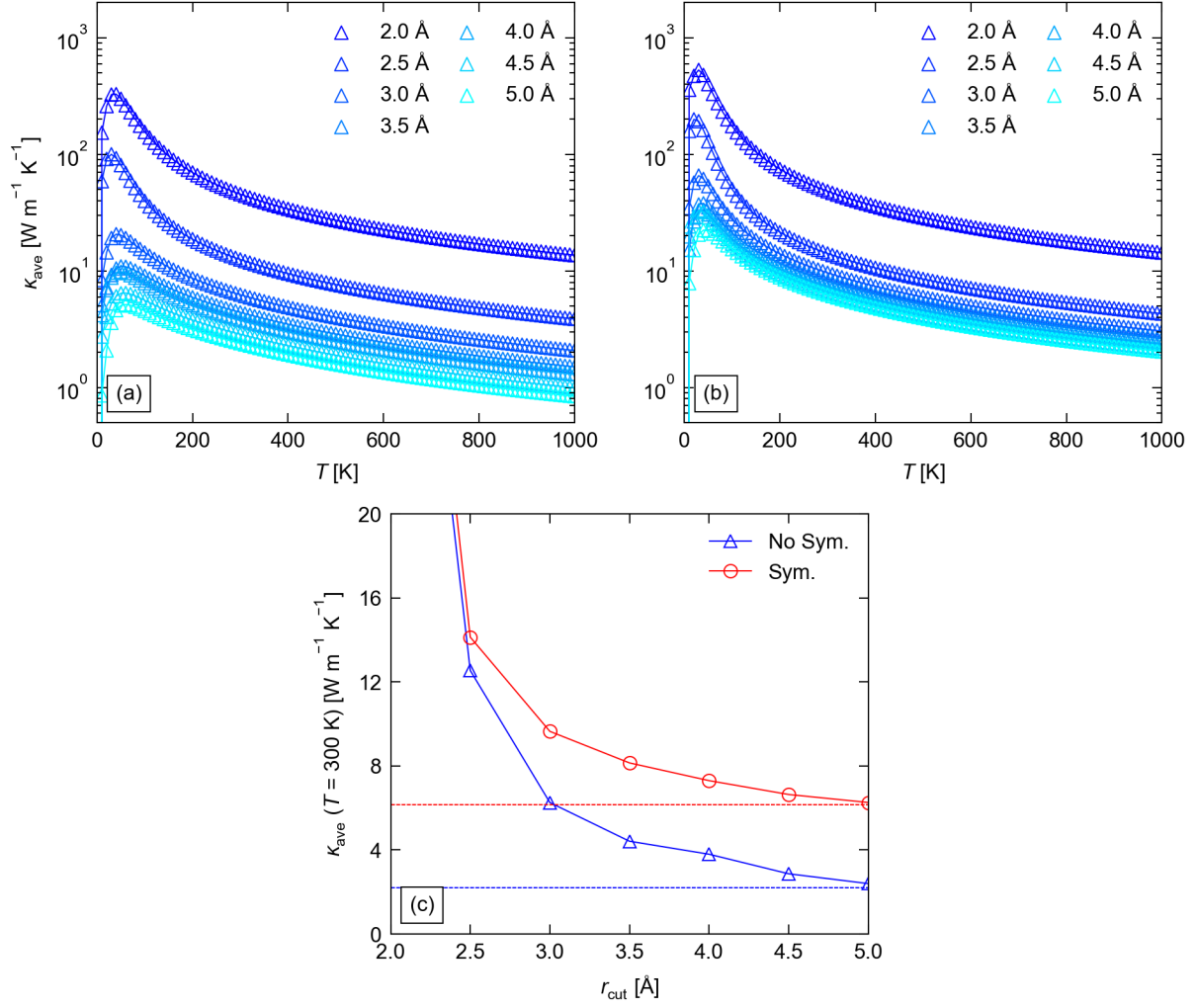
Figure S10: Convergence of the averaged lattice thermal conductivity of LiNiO$_2$ (2×10^{-2} Å displacement step) as a function of the 3rd-order interaction cutoff r_{cut}. (a)/(b) κ_{ave} as a function of temperature computed with $r_{\mathrm{cut}} = 2$-5 Å without (a) and with (b) symmetrisation applied to the IFCs to reduce numerical noise. (c) 300 K κ_{ave} as a function of r_{cut} computed with and without force-constant symmetrisation. The dashed lines show the reference values obtained using the full set of 3rd-order IFCs defined in our chosen supercells.

Figure S11: Convergence of the averaged lattice thermal conductivity of LiMnO$_2$ as a function of the 3rd-order interaction cutoff r_{cut}. (a)/(b) κ_{ave} as a function of temperature computed with r_{cut} = 2-5 Å without (a) and with (b) symmetrisation applied to the IFCs to reduce numerical noise. (c) 300 K κ_{ave} as a function of r_{cut} computed with and without force-constant symmetrisation. The dashed lines show the reference values obtained using the full set of 3rd-order IFCs defined in our chosen supercells.

Comparison of the relaxation-time approximation (RTA) to the full linearised Boltzmann transport equation (LBTE) solution

Table S6: Room-temperature (300 K) thermal conductivity of $LiCoO_2$, $LiNiO_2$ and $LiMnO_2$ computed using the relaxation-time approximation (RTA) and the full solution to the linearised Boltzmann trsnsport equation (LBTE). Both sets of calculations were performed using the lifetime-sampling meshes identified from the convergence tests in the first section, with forc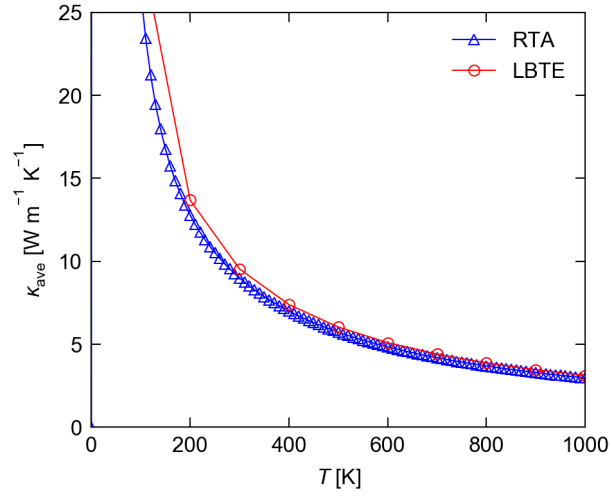e-constant symmetrisation applied to reduce numerical noise. The data for $LiNiO_2$ was obtained using the 3rd-order force constants calculated with a 2×10^{-2} Å finite-displacement step size.

System	Method	κ_{xx}	κ_{yy}	κ_{zz}	κ_{ave}
$LiCoO_2$	RTA	66.0	-	11.5	47.8
	LBTE	77.6	-	11.7	55.6
$LiNiO_2$	RTA	3.27	9.39	5.81	6.16
	LBTE	3.55	11.6	6.98	7.38
$LiMnO_2$	RTA	16.7	5.69	4.58	8.99
	LBTE	18.1	5.87	4.60	9.53
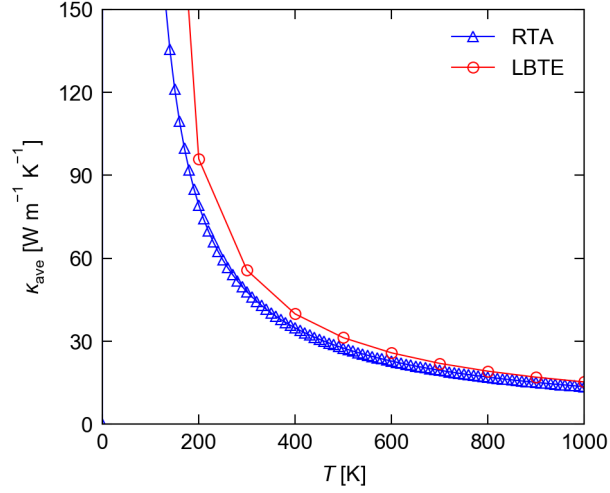
Figure S12: Comparison of the averaged thermal conductivity κ_{ave} of LiCoO$_2$ as a function of temperature, computed from the relaxation-time approximation (RTA) and the full solution to the linarised Boltzmann transport equation (LBTE). Both calculations were performed using a $15 \times 15 \times 15$ lifetime-sampling mesh identified based on the convergence tests in the first section, with force-constant symmetrisation applied to reduce numerical noise.

Figure S13: Comparison of the averaged thermal conductivity κ_{ave} of LiNiO$_2$ (2×10^{-2} Å displacement step) as a function of temperature, computed from the relaxation-time approximation (RTA) and the full solution to the linarised Boltzmann transport equation (LBTE). Both calculations were performed using a $15 \times 15 \times 15$ lifetime-sampling mesh identified based on the convergence tests in the first section, with force-constant symmetrisation applied to reduce numerical noise.

Figure S14: Comparison of the averaged thermal conductivity κ_{ave} of $LiMnO_2$ as a function of temperature, computed from the relaxation-time approximation (RTA) and the full solution to the linarised Boltzmann transport equation (LBTE). Both calculations were performed using a $16 \times 8 \times 4$ lifetime-sampling mesh identified based on the convergence tests in the first section, with force-constant symmetrisation applied to reduce numerical noise.

Anisotropy in the lattice thermal conductivity of LiCoO$_2$, LiNiO$_2$ and LiMnO$_2$
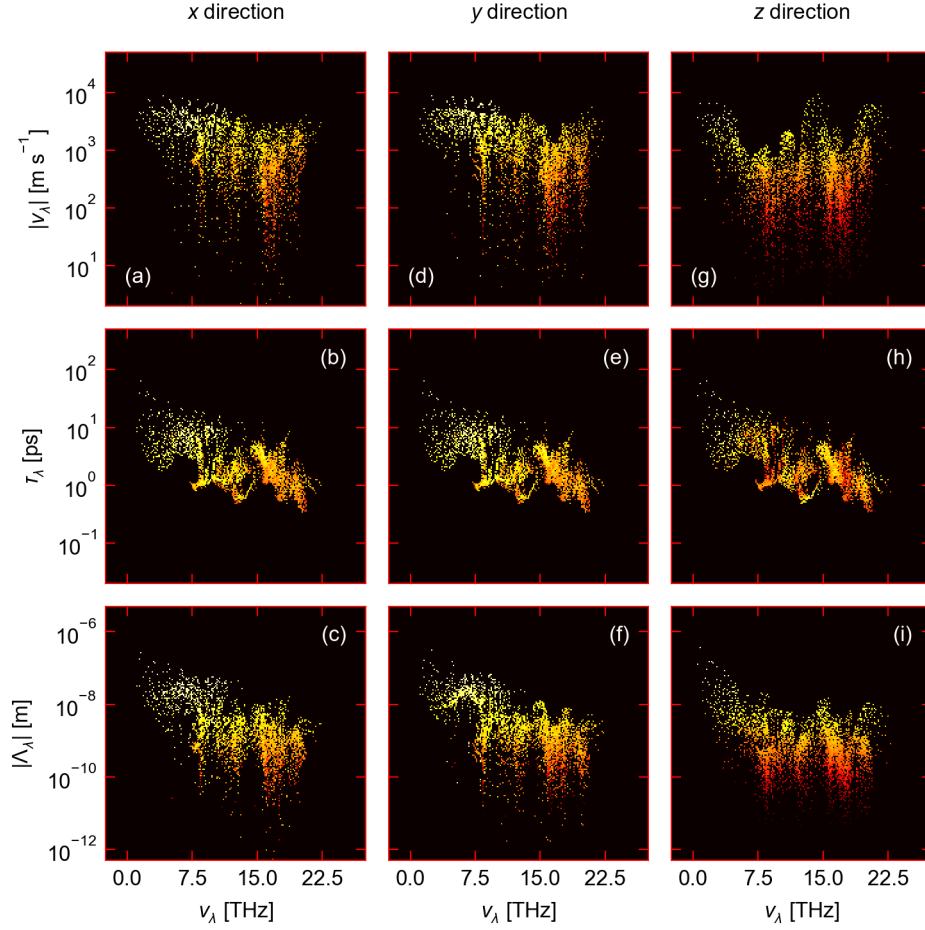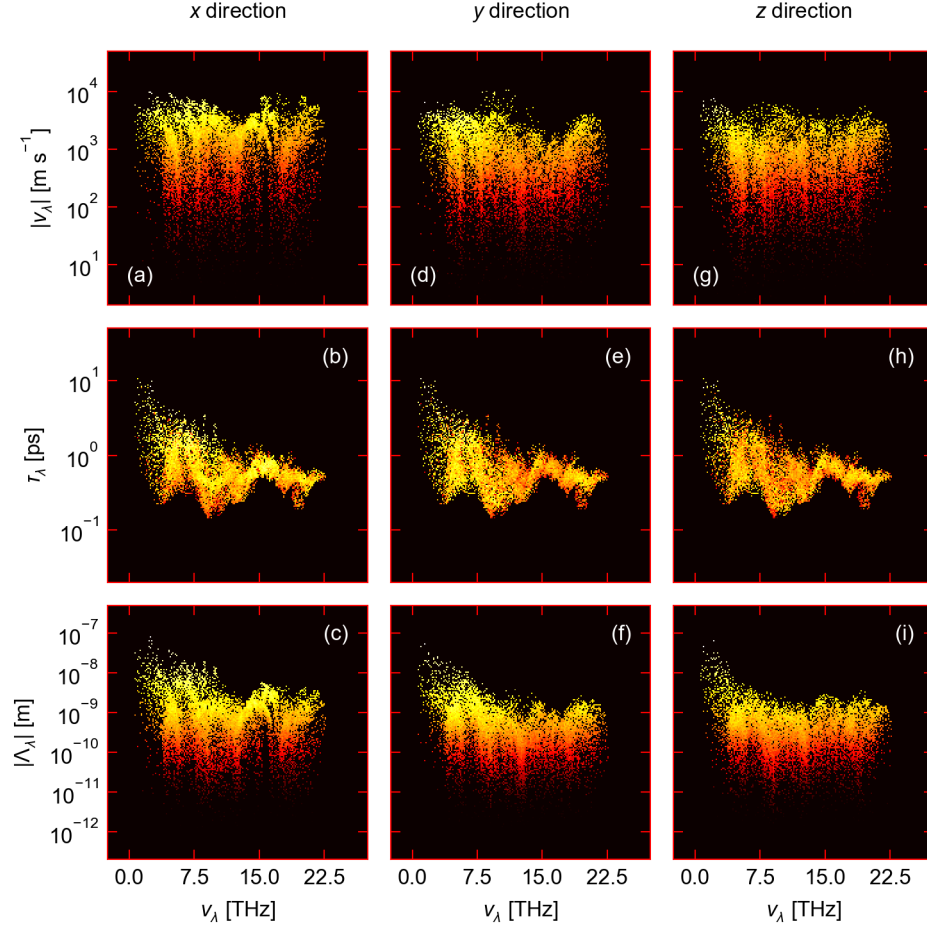

Figure S15: Analysis of the 300 K thermal conductivity in LiCoO$_2$ along the principal Cartesian directions x (a-c), y (d-f), and z (g-i). The top row (a, d, g) shows the frequency spectra of the phonon mode group velocities $|\nu_\lambda|$, the central row (b, e, h) shows the phonon lifetimes τ_λ, and the bottom row (c, f, i) shows the phonon mean-free paths $|\Lambda_\lambda|$. The heat map is coloured from red to yellow based on the modal contributions to the thermal conductivity tensor along the Cartesian directions, i.e. κ_{xx}, κ_{yy}. κ_{zz}.
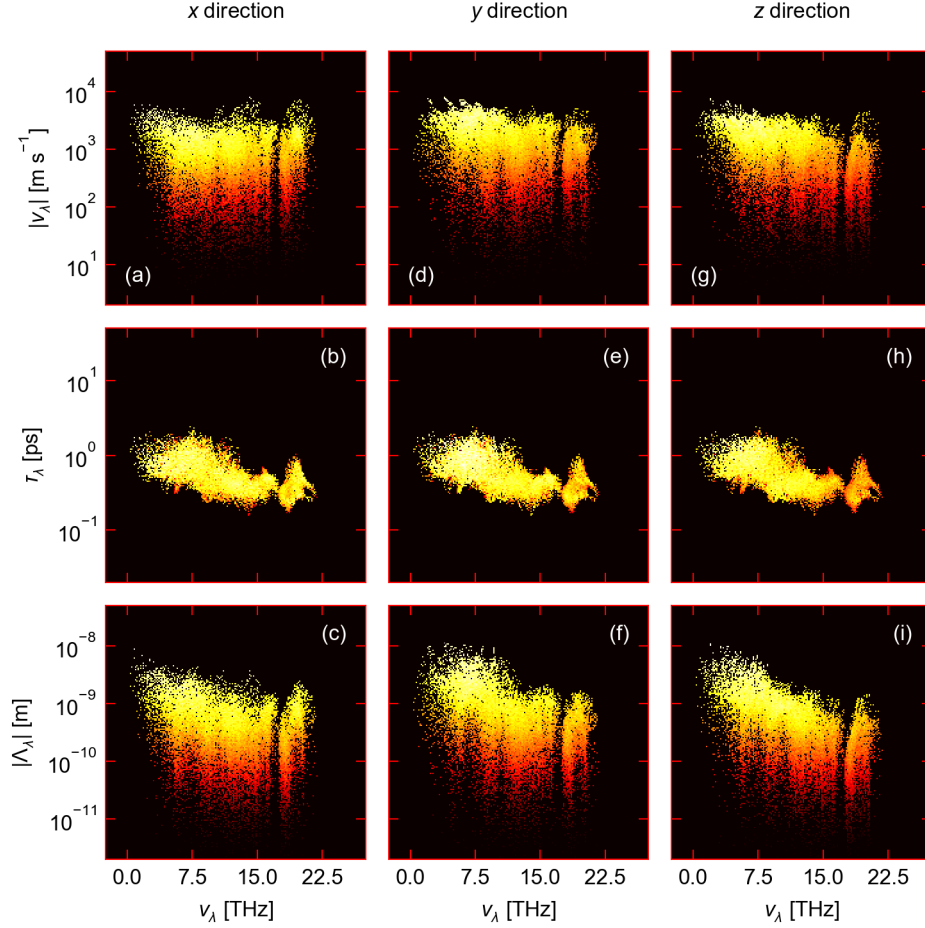
Figure S16: Analysis of the 300 K thermal conductivity in LiNiO$_2$ along the principal Cartesian directions x (a-c), y (d-f), and z (g-i). The top row (a, d, g) shows the frequency spectra of the phonon mode group velocities $|\nu_\lambda|$, the central row (b, e, h) shows the phonon lifetimes τ_λ, and the bottom row (c, f, i) shows the phonon mean-free paths $|\Lambda_\lambda|$. The heat map is coloured from red to yellow based on the modal contributions to the thermal conductivity tensor along the Cartesian directions, i.e. κ_{xx}, κ_{yy}. κ_{zz}.

Figure S17: Analysis of the 300 K thermal conductivity in $LiMnO_2$ along the principal Cartesian directions x (a-c), y (d-f), and z (g-i). The top row (a, d, g) shows the frequency spectra of the phonon mode group velocities $|\nu_\lambda|$, the central row (b, e, h) shows the phonon lifetimes τ_λ, and the bottom row (c, f, i) shows the phonon mean-free paths $|\Lambda_\lambda|$. The heat map is coloured from red to yellow based on the modal contributions to the thermal conductivity tensor along the Cartesian directions, i.e. κ_{xx}, κ_{yy}. κ_{zz}.

Cumulative thermal conductivity of LiCoO$_2$, LiNiO$_2$ and LiMnO$_2$ as a function of frequency
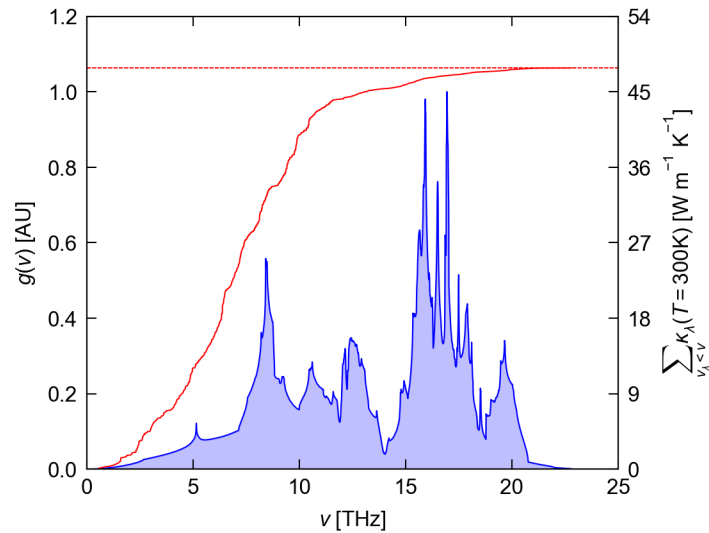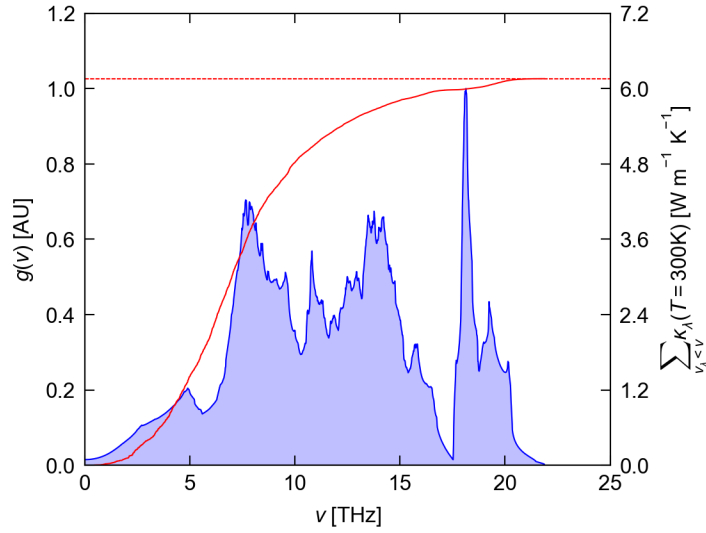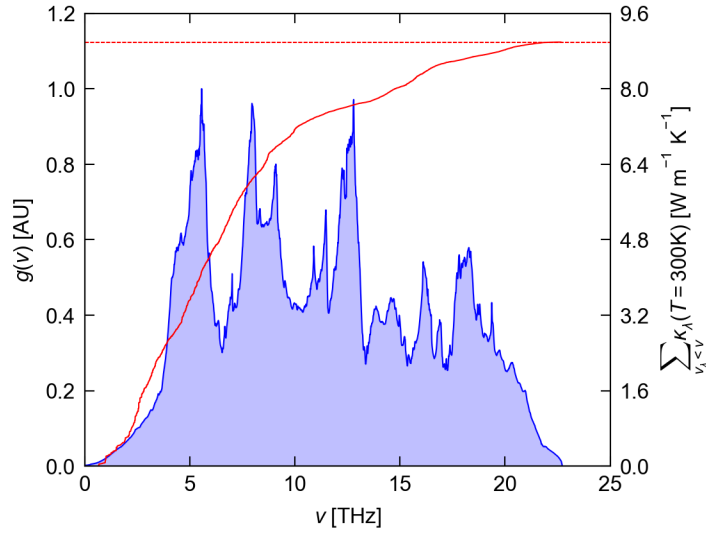

Figure S18: Comparison of the phonon density of states $g(\nu)$ (DoS, blue) and cumulative averaged lattice thermal conductivity as a function of frequency at $T = 300$ K (red) in LiCoO$_2$. The dashed red line shows the total κ_{ave} at 300 K for reference. The phonon DoS was calculated by interpolating the phonon frequencies onto a uniform Γ-centered grid of wavevectors with $48 \times 48 \times 48$ subdivisions and using the linear tetrahedron method for Brillouin-zone integration.

Figure S19: Comparison of the phonon density of states $g(\nu)$ (DoS, blue) and cumulative averaged lattice thermal conductivity as a function of frequency at $T = 300$ K (red) in LiNiO$_2$. The dashed red line shows the total κ_{ave} at 300 K for reference. The phonon DoS was calculated by interpolating the phonon frequencies onto a uniform Γ-centered grid of wavevectors with $48 \times 48 \times 48$ subdivisions and using the linear tetrahedron method for Brillouin-zone integration.

Figure S20: Comparison of the phonon density of states $g(\nu)$ (DoS, blue) and cumulative averaged lattice thermal conductivity as a function of frequency at $T = 300$ K (red) in LiMnO$_2$. The dashed red line shows the total κ_{ave} at 300 K for reference. The phonon DoS was calculated by interpolating the phonon frequencies onto a uniform Γ-centered grid of wavevectors with $48 \times 24 \times 12$ subdivisions and using the linear tetrahedron method for Brillouin-zone integration.

Effect of grain size on the thermal conductivity of LiCoO$_2$, LiNiO$_2$ and LiMnO$_2$
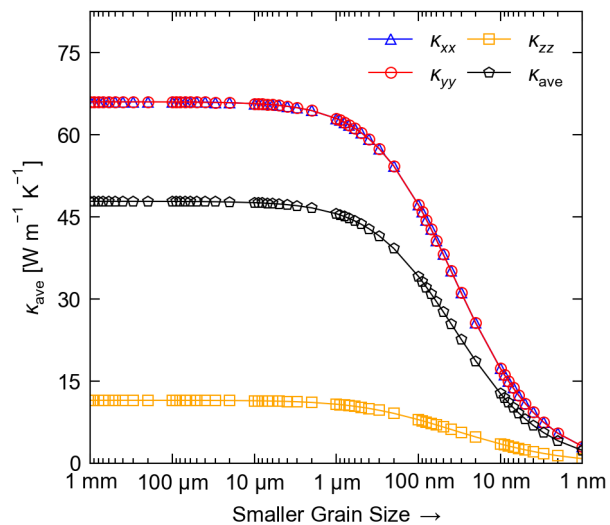

Figure S21: Effect of grain size on the 300 K thermal conductivity κ of LiCoO$_2$ along the principal Cartesian directions (κ_{xx}, κ_{yy} and κ_{zz}) and on the average thermal conductivity κ_{ave}.
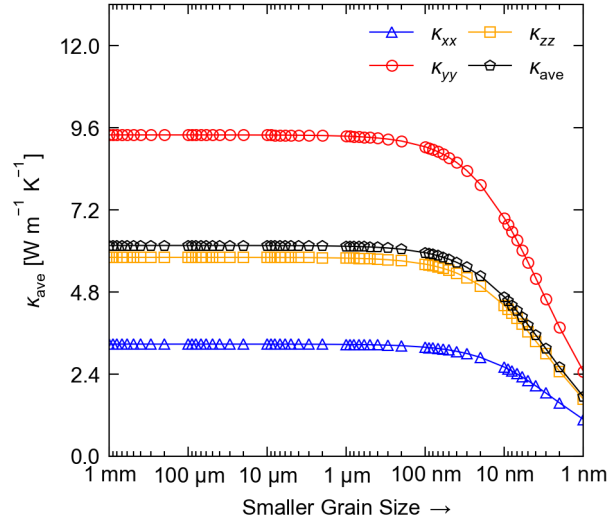
Figure S22: Effect of grain size on the 300 K thermal conductivity κ of LiNiO$_2$ along the principal Cartesian directions (κ_{xx}, κ_{yy} and κ_{zz}) and on the average thermal conductivity κ_{ave}.
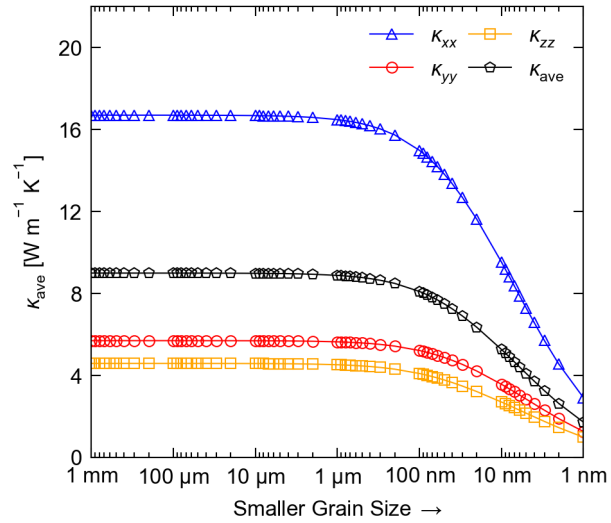
Figure S23: Effect of grain size on the 300 K thermal conductivity κ of LiMnO$_2$ along the principal Cartesian directions (κ_{xx}, κ_{yy} and κ_{zz}) and on the average thermal conductivity κ_{ave}.

Effect of transition metal mass variation on thermal transport
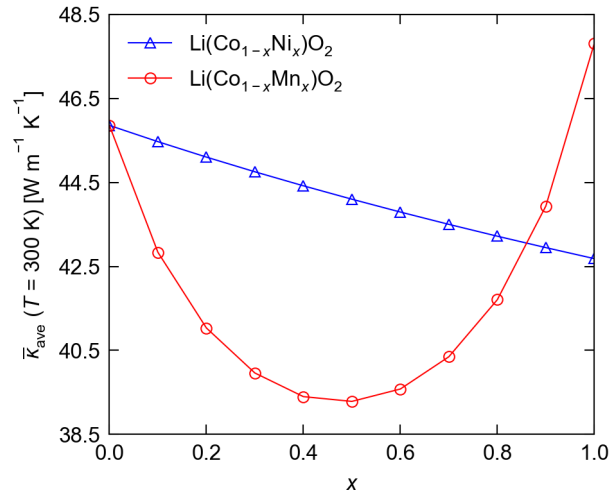
Figure S24: Averaged thermal conductivity $\overline{\kappa}_{ave}$ as a function of composition in the hypothetical binary alloys $Li(Co_{1-x}Ni_x)O_2$ and $Li(Co_{1-x}Mn_x)O_2$. As described in the text, $\overline{\kappa}$ is calculated assuming that the alloy remains in the $LiCoO_2$ structure and that the primary affect of the metal substitution on the thermal transport is the change in average mass and mass variance.
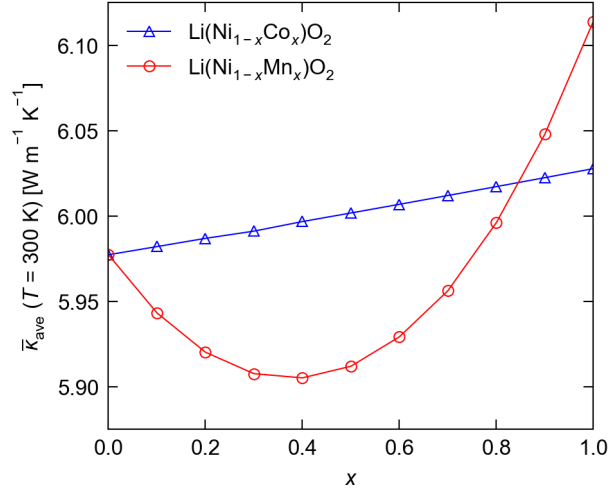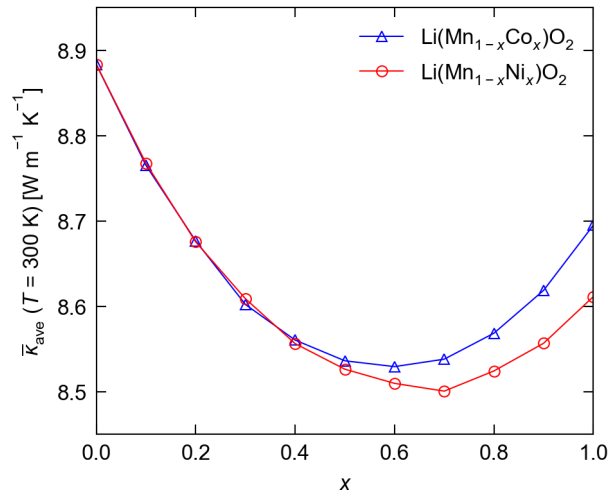
Figure S25: Averaged thermal conductivity $\overline{\kappa}_{\mathrm{ave}}$ as a function of composition in the hypothetical binary alloys $\mathrm{Li(Ni_{1-x}Co_x)O_2}$ and $\mathrm{Li(Ni_{1-x}Mn_x)O_2}$. As described in the text, $\overline{\kappa}$ is calculated assuming that the alloy remains in the $\mathrm{LiNiO_2}$ structure and that the primary affect of the metal substitution on the thermal transport is the change in average mass and mass variance.

Figure S26: Averaged thermal conductivity $\overline{\kappa}_{\mathrm{ave}}$ as a function of composition in the hypothetical binary alloys $\mathrm{Li(Mn_{1-x}Co_x)O_2}$ and $\mathrm{Li(Mn_{1-x}Ni_x)O_2}$. As described in the text, $\overline{\kappa}$ is calculated assuming that the alloy remains in the $\mathrm{LiMnO_2}$ structure and that the primary affect of the metal substitution on the thermal transport is the change in average mass and mass variance.
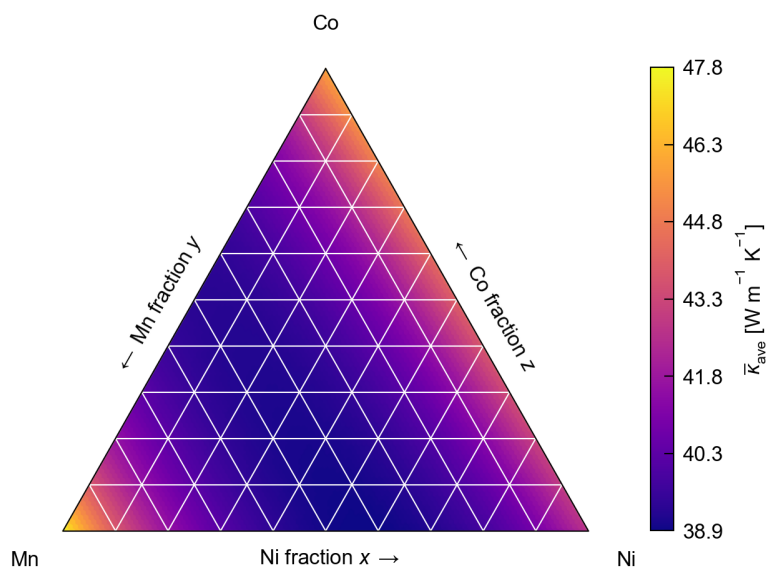
Figure S27: Averaged thermal conductivity $\overline{\kappa}_{\mathrm{ave}}$ as a function of composition in the hypothetical ternary alloy $\mathrm{Li(Ni_xMn_yCo_z)O_2}$ $(x + y + z = 1)$ in the $\mathrm{LiCoO_2}$ structure. As described in the text, $\overline{\kappa}$ is calculated assuming the primary affect of the metal substitution on the thermal transport is the change in average mass and mass variance.
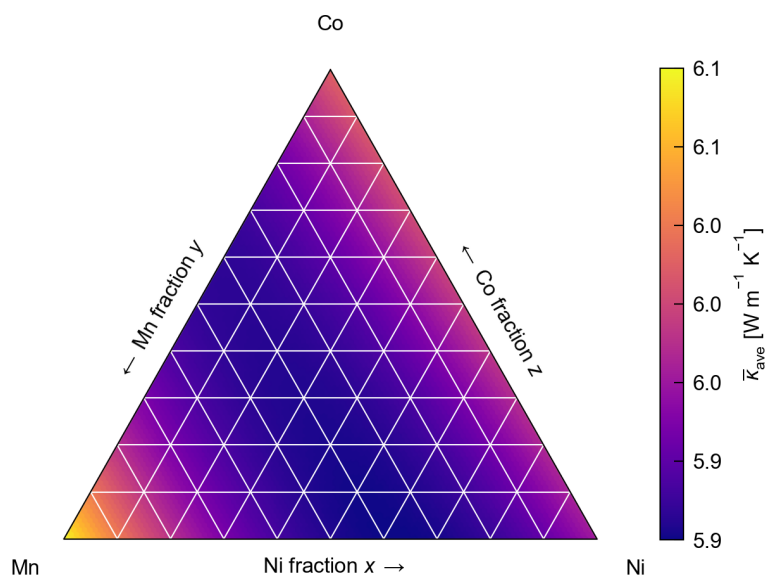

Figure S28: Averaged thermal conductivity $\overline{\kappa}_{\mathrm{ave}}$ as a function of composition in the hypothetical ternary alloy $\mathrm{Li(Ni_xMn_yCo_z)O_2}$ $(x + y + z = 1)$ in the $\mathrm{LiNiO_2}$ structure. As described in the text, $\overline{\kappa}$ is calculated assuming the primary affect of the metal substitution on the thermal transport is the change in average mass and mass variance.
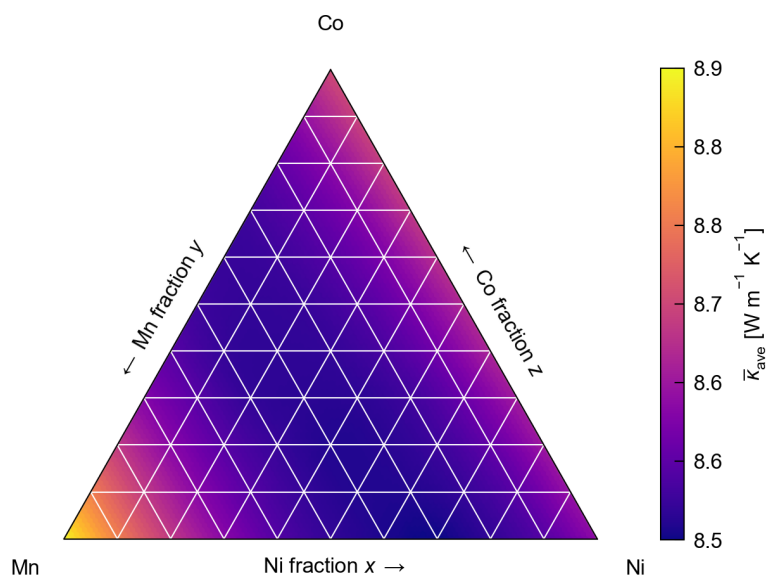
Figure S29: Averaged thermal conductivity $\overline{\kappa}_{\mathrm{ave}}$ as a function of composition in the hypothetical ternary alloy $\mathrm{Li(Ni_xMn_yCo_z)O_2}$ $(x + y + z = 1)$ in the $\mathrm{LiMnO_2}$ structure. As described in the text, $\overline{\kappa}$ is calculated assuming the primary affect of the metal substitution on the thermal transport is the change in average mass and mass variance.